Unconventionally Polarized Sources for Remote Aerosol Sensing

Brandon G. Zimmerman
National Aeronautics and Space Administration
Goddard Space Flight Center
Greenbelt, MD, USA
brandon.g.zimmerman@nasa.gov

Thomas G. Brown
The Institute of Optics
University of Rochester
Rochester, NY, USA

Abstract - *We introduce a class of unconventional, spatially inhomogeneous polarized beams for their application in aerosol remote sensing and polarimetry. One such beam may be formed by the unique superposition of right and left circularly polarized beams by a customized Nomarski prism. Such superposition results in a beam that repeatedly traverses the equator of the Poincaré sphere in one of the beam's spatial dimensions, such that, an image of light scattered from the beam yields the phase functions of the scatterers without temporal modulation of the input polarization. We call this a One Dimensional Poincaré Beam. We show that by illuminating an ensemble of Mie scatterers with our beam, that we can extract the phase functions, and size of the scatterers (amongst other physical parameters), in a manner that is both faster and more efficient than conventional methods and shows promise as a suitable instrument for integrating on aircraft modules for in-situ aerosol remote sensing measurements.*

Keywords: Aerosol remote sensing, polarimetry, Mie scatterer, One Dimensional Poincaré Beam.

1 Introduction and Background

Concerns about natural and anthropogenic influences on climate and the accuracy of climate models have spawned an increased interest in polarimetric imaging to characterize the scattering from aerosols, ice, and cloud particles. The characterizations of such aerosols in our atmosphere are determined by the polarimetric properties we are able to retrieve upon optical scattering. Accurate modeling of these aerosols allows us to answer common and current environmental concerns such as: How can we more accurately retrieve aerosol particle properties from polarimetric remote sensing measurements? What are the true scattering properties of natural and anthropogenic aerosol particles over particular regions of interest? What are their specific roles in the climate change of those particular regions? The foundation of these measurements can be reviewed in [1-5]. Today, imaging polarimetry has become a standard technique for modern polarimetry and particle characterization [6, 7]; however, there is always a need for advanced polarimetric measurement techniques [8, 9]. This paper will provide an overview of an emerging field of unconventional polarimetric techniques to be utilized when measuring the polarized fields generated small particles.

Knowledge of the details of energy transfer, climate, or characterization of particle pollutants requires knowledge of the optical properties of the particles. The angular dependence of the linear and circular polarization of scattered light from clouds and aerosols can be used to characterize the size distribution, complex refractive indices, shape, and orientation of the particles making up that aerosol as well as the visibility, light propagation, and radiant transfer of light passing through it [10-13].

Conventional remote polarimetric techniques typically consist of temporally modulating a linear polarizer between a series of standard orientations (e.g., 0, 45, 90, and 135 degrees) [7]. Several images at each of these analyzer orientations are required to characterize the phase function parameters of the particle ensemble [6]. The temporal modulation of these linear input polarization states slows down the measurements, can introduce erroneous polarization signatures corrupting the data, and furthermore requires careful synchronization between source and camera [6].

We define an unconventionally polarized source as a light field that departs from uniformly polarized, beam-like descriptions [14]. One such beam can be formed by the superposition of equal amplitude right and left circularly polarized light with a small angular shear between the two beams as below in Figure 1. The result is a beam with a spatially varying polarization signature that spans all of the linear polarization states on the Poincare sphere. We demonstrate that by illuminating an ensemble of Mie scatterers with such a beam, one can characterize the physical properties of the ensemble in fewer measurements than the conventional temporal methods, while furthermore ridding the technique of the time synchronous errors also associated with temporal methods.

2 A One Dimensional Poincaré Beam

The electric field resulting from the superposition of any two polarized plane waves can be written using Jones vectors

$$\mathrm{E}(\boldsymbol{r}) = \left(a_1 e^{i\mathbf{k_1}\cdot\mathbf{r}} \begin{bmatrix} e_x \\ e_y \end{bmatrix}_1 + a_2 e^{-i\mathbf{k_2}\cdot\mathbf{r}} \begin{bmatrix} e_x \\ e_y \end{bmatrix}_2 \right) \quad (1)$$

where a_j and $\mathbf{k}_j$ represent the amplitude and paraxial wave vector of the jth wave, respectively. It can be symmetrized in the following form:

$$\mathrm{E}(\boldsymbol{r}) = e^{i\bar{\mathbf{k}}\cdot\mathbf{r}} \left(a_1 e^{i\Delta\mathbf{k}\cdot\mathbf{r}} \begin{bmatrix} e_x \\ e_y \end{bmatrix}_1 + a_2 e^{-i\Delta\mathbf{k}\cdot\mathbf{r}} \begin{bmatrix} e_x \\ e_y \end{bmatrix}_2 \right) \quad (2)$$

where $\bar{\mathbf{k}} = 0.5(\mathbf{k}_1 + \mathbf{k}_2)$ and $\boldsymbol{\Delta\mathbf{k}} = 0.5(\mathbf{k}_1 - \mathbf{k}_2)$. We now suppose that the two wave vectors lie in the x-z plane and are oriented so that the z axis bisects the two waves as shown in Figure 1.

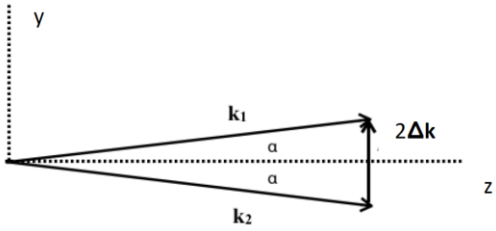

Figure 1. Geometry of plane wave intersection.

We suppose that the two beams are now Gaussian, and intersect with an angular shear 2α, which can be represented in the global phase term, φ(y) as:

$$\varphi(y) = \Delta\mathbf{k}\cdot\mathbf{r} = \frac{2\pi\alpha y}{\lambda}. \quad (3)$$

If the polarizations are the same, the result is a spatially homogeneous polarized beam (Figure 2).

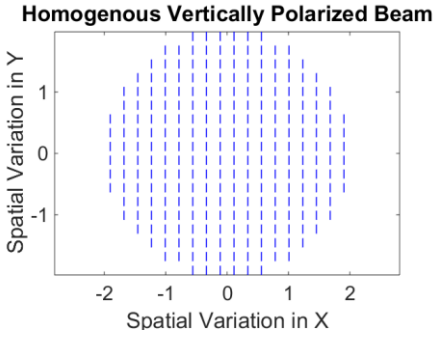

Figure 2. Cross section of a homogeneous vertically polarized beam.

If the amplitudes are equal but the polarizations are orthogonal right and left circular, the Jones vector representation of the plane wave interference expression becomes

$$\frac{1}{2}\left(e^{i\varphi(\mathrm{y})} \begin{bmatrix} 1 \\ -i \end{bmatrix} + e^{-i\varphi(\mathrm{y})} \begin{bmatrix} 1 \\ i \end{bmatrix} \right) = \begin{bmatrix} \cos(\varphi(\mathrm{y})) \\ \sin(\varphi(\mathrm{y})) \end{bmatrix}. \quad (4)$$

As a result, the spatial variation of the phase term results in a spatial variation of the electric field components in one dimension. The equal amplitude components of both right and left circular polarized beams map the polarization states of this beam repeatedly around a closed loop on the Poincaré sphere over a single fringe period, and thus we term this beam a One Dimensional Poincaré Beam (ODPB). The spatial polarization properties of this beam can be modeled by plotting the electric vector field or the Stokes parameters over a single fringe period as shown in Figure 3 below.

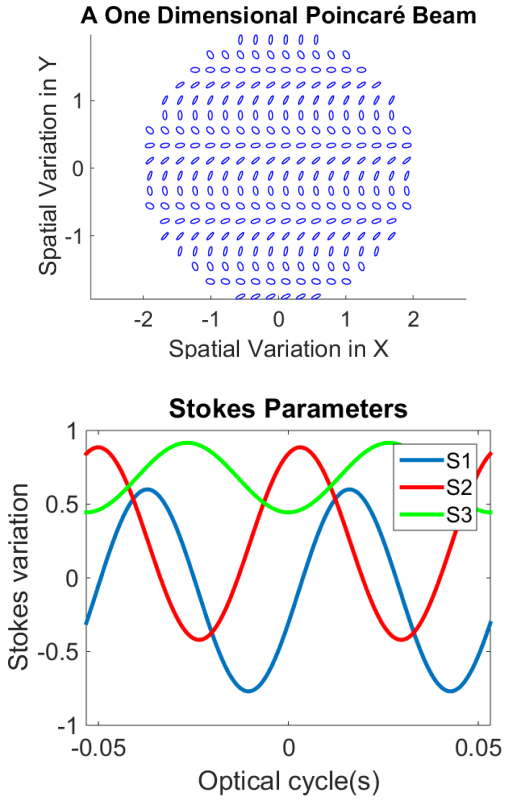

Figure 3. Spatial variation of a one dimensional Poincaré beam as shown by plotting the electric field vectors (top) and Stokes parameters (bottom) over an optical cycle.

The sinusoidal Jones vector components in Equation 5 allow us to represent the beam with the following input Stokes vector

$$S_{in} = \begin{bmatrix} 1 \\ \cos(2\Delta k y) \\ \sin(2\Delta k y) \\ S_3 \end{bmatrix} I_o, \quad (5)$$

where Δk is the scalar (y)-component of **Δk** along a line perpendicular to the interference fringes, and assuming a fully polarized beam, $S_3=\sqrt{1-\cos(2\Delta k y)^2-\sin(2\Delta k y)^2}$.

3 Mie Scattering from a One Dimensional Poincaré Beam

A ODPB incident upon an ensemble of spherically symmetric particles and detected by a linear analyzer can be represented by the following scattering matrix expression

$$\boldsymbol{S}_{out} = \frac{1}{2}\begin{bmatrix} 1 & cos2\theta_A & sin2\theta_A & 0 \\ cos2\theta_A & cos^2 2\theta_A & sin2\theta_A cos2\theta_A & 0 \\ sin2\theta_A & sin2\theta_A cos2\theta_A & sin^2 2\theta_A & 0 \\ 0 & 0 & 0 & 0 \end{bmatrix} \times \begin{bmatrix} p_{11} & p_{12} & 0 & 0 \\ p_{12} & p_{22} & 0 & 0 \\ 0 & 0 & p_{33} & p_{34} \\ 0 & 0 & p_{-34} & p_{33} \end{bmatrix} \mathbf{S}_{in}, \quad (6)$$

where the input Stokes parameters are represented by a matrix of Stokes vectors

$$\mathbf{S}_{in} = \begin{bmatrix} 1 & 1 & 1 & \dots \\ S_1(y_1) & S_1(y_2) & S_1(y_3) & \dots \\ S_2(y_1) & S_2(y_2) & S_2(y_3) & \dots \\ S_3(y_1) & S_3(y_2) & S_3(y_3) & \dots \end{bmatrix} I_o(y_j)$$

such that each column represents j_{th} (pixel) in the horizontal direction of the image. The intensity of the scattered light, *I(x)* recorded at the detector then becomes:

$$I(y) = I_o(y_j)(p_{11} + p_{12}S_1(y) + (p_{21} + p_{22}S_1(y))cos2\theta A + (p_{33}S_2(y) + p_{34}S_3(y))sin2\theta A). \quad (7)$$

where θA is the transmission axis orientation of the analyzer and the phase functions that physically characterize the scatterers are represented by the phase matrix **P**. Each element of the phase matrix p_{mn} provides a different physical description of the scatterer and is dependent on the polar scattering angle θ. Distinct analyzer orientations of H(θA=0), V(θA=π/2), P(θA=π/4), and M(θA=3π/4), respectively, yield the following system of equations to describe the scattered signal received by the detector,

$$I_h(y) = I_o(y_j)(p_{11} + p_{12}S_1(y) + p_{21} + p_{22}S_1(y))$$
$$I_v(y) = I_o(y_j)(p_{11} + p_{12}S_1(y) - (p_{21} + p_{22}S_1(y))$$
$$I_p(y) = I_o(y_j)(p_{11} + p_{12}S_1(y) + p_{33}S_2(y) + p_{34}S_3(y))$$
$$I_m(y) = I_o(y_j)(p_{11} + p_{12}S_1(y) - p_{33}S_2(y) - p_{34}S_3(y)), \quad (8)$$

where I_h(I_v) represent the horizontal(vertical) irradiances and I_p(I_m) the $\pm 45^\circ$ linearly polarized irradiances, respectively. It should be observed here that sinusoidal varying spatial signature of our beam, allows one to capture all of the phase functions that describe the scatterers in 4 images.

4 Experimental Setup

4.1 Sample preparation

The scattering samples used in this experiment are polystyrene latex spheres having nominal diameters of 820 nm (3% dispersion factor) and 1 μm (3% dispersion factor). The spheres were manufactured by Duke Scientific. Each sample is drawn by a micropipette and dispersed in a deionized (DI) water solution. This solution is then placed in an ultrasound bath for approximately 15-20 minutes to disperse any particle clumping. Particle clumping can result in non-spherical particle arrangements, as well as in non-uniform size distribution; either of these would represent a departure from the homogeneous spherical particle approximation.

4.2 Beam preparation

A photograph of the experimental layout is shown in Figure 4. A Melles Griot frequency doubled Nd:YAG laser (~2 Watts at a wavelength of 532 nm) **(A)** is passed through a spatial filter and collimating lens **(B)** to produce a collimated Gaussian beam. The spatial filter consists of a pinhole placed in the focal plane of a microscope objective. The collimated beam (~ 5mm in diameter) is then passed through a Semrock linear analyzer **(C)** oriented at 45° such that the output is a linearly polarized beam of '*equal*' amplitude horizontal and vertical components. The beam is then incident upon a Nomarski prism and quarter wave plate **(D)** to produce the ODLPB. The ODLPB is then passed through three lenses: 1.) A 5x microscope objective configured to produce a very low numerical aperture focus at the sample: 2) a pair of cylindrical lenses **(E)** to expand and collimate the beam in the vertical direction, generating a thin sheet of light or *lightsheet* that is incident upon the scatterers.

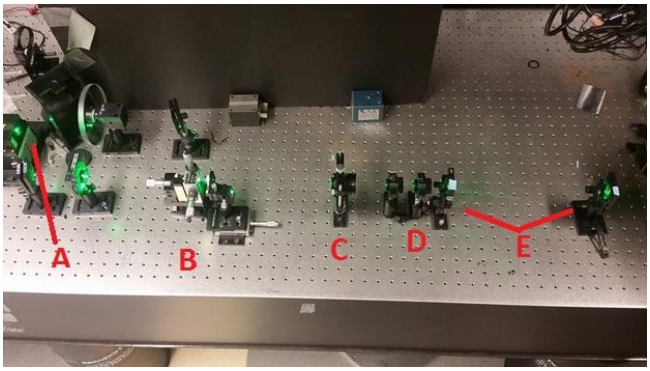

Figure 4. Experimental layout of beam generation path: A-532 nm laser source, B-spatial filter, C-Semrock polarizer oriented at +45 degrees, D-Nomarski prism followed by QWP, E-cylindrical beam expander.

The focus of the 5x objective lens is adjusted such that the beam waist is centered on the scattering cell shown in Figure 5, and the depth of focus extends through the field of view of the detection camera.

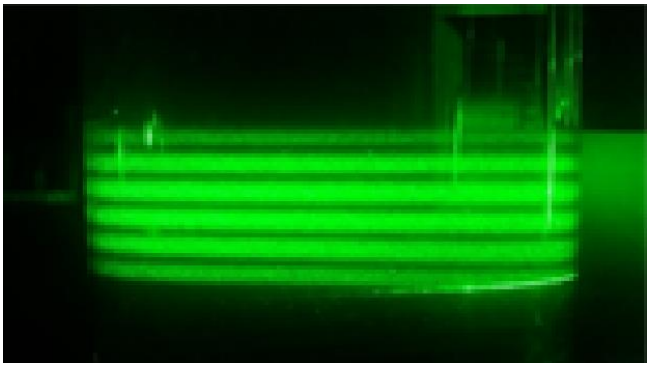

Figure 5. Ensemble of polystyrene latex spheres (PLS) illuminated by a ODPB inside a cylindrical scattering cell.

A similar technique is utilized in light sheet microscopy for improved resolution and sectioning of a sample, and thus we refer to this method as light sheet scatterometry.

4.3 Scattering geometry

Figure 6 shows a photograph of the scatterer and camera arrangement. The light sheet is focused at the center of a scattering cell **(F)** that sits in the center of a motorized rotation stage (Newport Corp 855C) equipped with a controller having a serial communications interface (RS232). A linear analyzer **(G)** is placed in front of a thin slit **(H)** to limit the range of collection angles. The camera **(I)** comprises an f=25 mm variable focus camera lens mounted to a CMOS camera (Imaging Source) capable of 12 bit image acquisition. The analyzer, slit, and camera are then mounted on a rotator arm that is attached to the rotation stage. The camera is focused at the center of the scattering cell **(J)** and rotated in increments of 2˚ from 20˚-156˚ in the polar scattering direction. By focusing the camera at the center of the rotation stage (coincides with the center of the scattering cell) we ensure that we are always imaging the same area of the scatterers and avoid any translation shifts of the image caused by rotating the camera. MATLAB is used to communicate with the 855C rotation stage as well as the camera, such that all camera rotations, image acquisitions, along with gain and exposure settings are automated by programs we have written. A full experiment consists of imaging the scatterers from 20˚-156˚ in the polar scattering direction with the analyzer set for H, V, P, and M in sequence. (The analyzer positions are set manually.) Each polarization image has the same gain and exposure settings for a given angle since the recovery algorithm requires taking accurate difference images. To ensure this, the first data set is taken with analyzer orientation set for V using a precalibrated series of gains and exposures. A set of logical conditions then ensure the same gain and exposure conditions for each subsequent run. Figure 6 shows a photograph of the experimental setup used for retrieving the scattered signal.

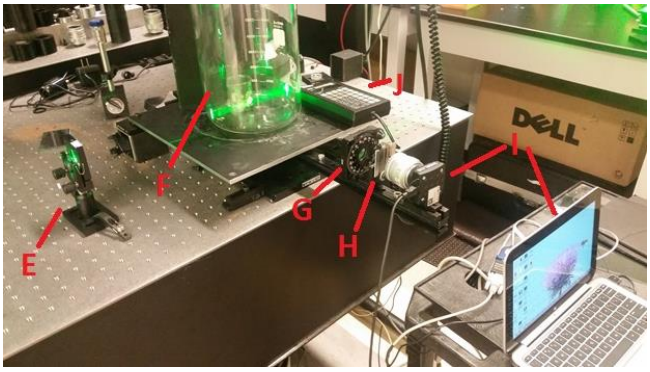

Figure 6. Experimental layout of scattering cell and detector elements: E-cylindrical beam expander, F-scattering cell, G-linear analyzer, H-thin slit, I-CCD camera automated by computer, J-rotation stage controller automated by computer.

5 Experimental Phase Function Acquisition

Given the Stokes parameters of the input beam, Equations 9 establish a system of equations that we now present in matrix form:

$$\begin{bmatrix} I_h(\mathrm{y}_j) \\ I_v(\mathrm{y}_j) \\ I_p(\mathrm{y}_j) \\ I_m(\mathrm{y}_j) \end{bmatrix} = \begin{bmatrix} 1 & S_1(\mathrm{y}_j) & 1 & S_1(\mathrm{y}_j) & 0 & 0 \\ 1 & S_1(\mathrm{y}_j) & -1 & -S_1(\mathrm{y}_j) & 0 & 0 \\ 1 & S_1(\mathrm{y}_j) & 0 & 0 & S_2(\mathrm{y}_j) & S_3(\mathrm{y}_j) \\ 1 & S_1(\mathrm{y}_j) & 0 & 0 & -S_2(\mathrm{y}_j) & -S_3(\mathrm{y}_j) \end{bmatrix} \begin{bmatrix} p_{11} \\ p_{12} \\ p_{21} \\ p_{22} \\ p_{33} \\ p_{34} \end{bmatrix}. \quad (9)$$

For each pixel j, there are 4 equations and 6 unknowns. For $N \geq 2$ pixels, this provides an overdetermined system of 4N equations. By stacking the measured irradiance values in a 2N element column vector, **I**, and similarly stacking the matrix of input Stokes parameters into a 4Nx6 matrix **M**,

$$\mathbf{P} = \mathbf{M}^{-1}\mathbf{I}, \qquad (10)$$

where **P** is the solution vector and $\mathbf{M}^{-1}$ is the pseudo-inverse. The symmetry of the problem requires $p_{12} = p_{21}$; while it is common to assume this condition, to test the self-consistency of the method we will compute them separately.

6 Experimental Results

To recover the phase functions, Equation 9 is carried out at each scattering angle, and the output vector provides the experimental phase function value at that angle. Figures 7 and 8 show the acquired phase functions for a suspension of 820 nm diameter polystyrene spheres. These values are plotted against their corresponding theoretical phase functions (shown in black) predicted by Mie Theory. The p_{11} phase function is generated on a log scale, and shows the total scattered intensity as a function of scattering angle. The polarization dependent phase functions (p_{12}, p_{22}, p_{33} and p_{34}) are normalized to p_{11} at each angle and plotted separately.

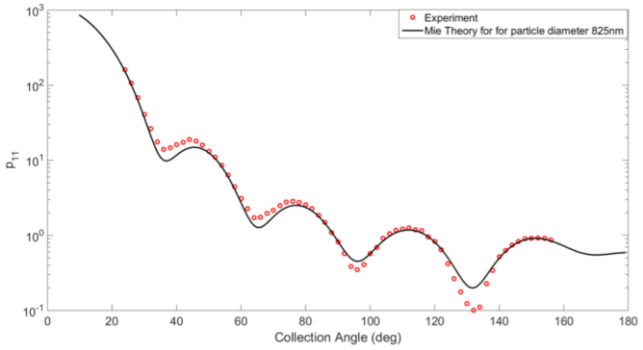

Figure 7. Experimental p_{11} (red) vs theoretical p_{11} (black) for 820 nm polystyrene latex spheres.

The same analysis is performed in Figures 9 and 10 for an ensemble of 1 micron particles.

In Figures 7 and 9, the scattered intensity, p_{11} shows both the bias in forward scattering, and the ripple structure associated with scattering particles larger than the wavelength. To show a quantitative comparison with Mie theory, p_{11} is globally scaled to the best fit overall scattering efficiency. p_{12} and p_{21}, although calculated independently, clearly satisfy the symmetry conditions that state these two should be equal. The p_{33} and p_{34} phase functions (Figures 8 and 10), while following the general form predicted by Mie theory, show a modulation depth that tends to either be steeper than the theoretical prediction (p_{33}) or more shallow (for p_{34}) than single scattering Mie theory predicts.

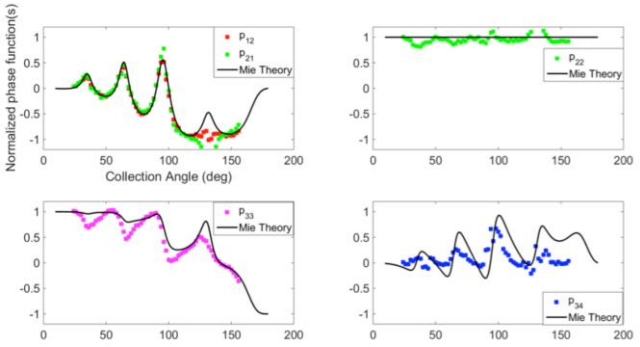

Figure 8. Experimental vs theoretical (black) phase functions for 820 nm polystyrene latex spheres.

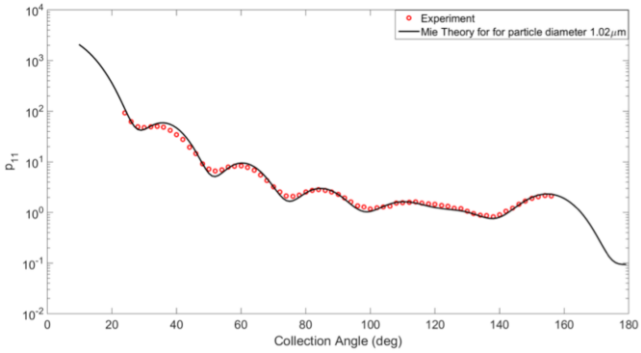

Figure 9. Experimental p_{11} (red) vs theoretical p_{11} (black) for 1 μm polystyrene latex spheres with DoP of 1.

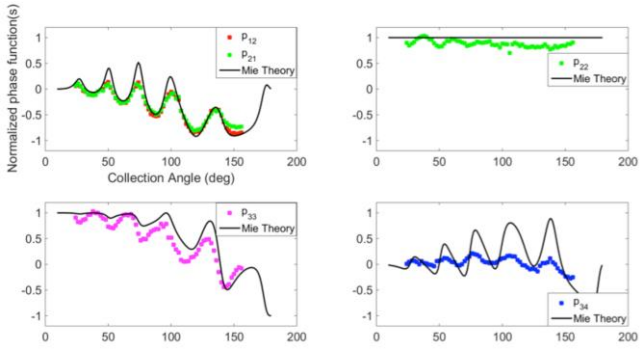

Figure 10. Experimental vs theoretical (black) phase functions for 1 μm polystyrene latex spheres with DoP of 1

The most notable difference between Mie theory and these experiments is clearly in the data for p_{34}. This is the component that connects circular polarization (S_3) to ±45 degree polarization (S_3) and is critically dependent on an accurate estimate of S_3. In the input beam. However, it was noted in section 2.3.4 that S_3 may be inferred from the linear polarizations while we can only do so by assuming a

particular *DoP*. While we are confident that the beam is fully polarized entering the solution, multiple scattering can yield a partially polarized illumination source at the point of observation. In such a case, the *DoP* would be less than 1, resulting in an overestimate of S_3.

We can test this hypothesis as follows: By adjusting the depolarization factor (*DoP*) in the analysis, we compare the phase functions. Figures 11 and 12 show the phase functions for particle diameters of 1 micron as the *DoP* decreases from 0.75 to 0.65.

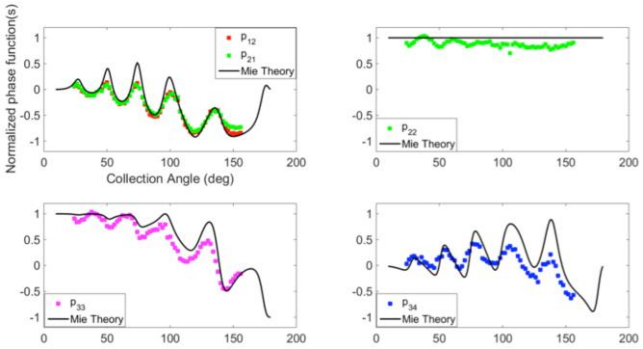

Figure 11. Experimental vs theoretical (black) phase functions for 1 µm polystyrene latex spheres with a DoP of 0.75.

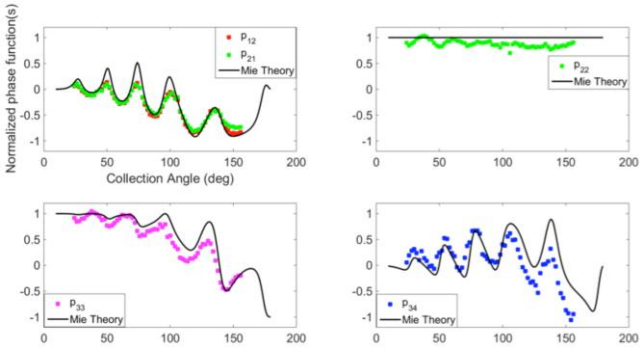

Figure 12. Experimental vs theoretical (black) phase functions for 1 µm polystyrene latex spheres with a DoP of 0.65.

As the DoP is changed, we see that the ripple structure in the p_{34} phase function is significantly affected (with little change to the other phase functions), indicating that there is likely a depolarization factor in the experiment. At this point we are unable to discern how much of this depolarization is due to multiple scattering, or to an unpolarized background signature created by the geometry of the experimental setup.

7 Qualifying the Method: Estimate of Particle Size

While polarimetric information is not required for particle sizing, the inclusion of p_{11} in the measurement allows us to test the method against conventional scattering measurements using known particle sizes while comparing with the predictions of Mie Theory. To do so, we define a merit function that tests the ratio of the experimentally recovered values of p_{11} to those predicted by Mie Theory. The error function is defined as:

$$\frac{1}{N}\sum_{n=1}^{N}\left(1-\frac{\frac{p_{11_{exp}}}{p_{11_{theory}}}}{mean\left(\frac{p_{11_{exp}}}{p_{11_{theory}}}\right)}\right)^2 \qquad (11)$$

where N is the number of data points that are experimentally represented by the discrete scattering angles, and $p_{11_{exp}}$ and $p_{11_{theory}}$ are the experimental and theoretical p_{11} phase function values, respectively. This expression is chosen for two reasons: 1) since we do not calibrate the absolute intensity of the measurement, this includes an implicit scaling factor; 2) by measuring the normalized root mean squared deviation of the ratio between theory and experiment, the p_{11} phase function can vary over many orders of magnitude while assuring equal weight on all angles.

The procedure is then as follows: A nominal particle diameter is chosen (e.g., 820 nm), and a $\pm 10\%$ range of diameter sizes is generated around the nominal size. A set of theoretical phase functions, $p_{11_{theory}}$, is generated using Mie Theory, for each particle diameter in the range established. Each data point is compared to its respective data point from the experimental p_{11} phase function, $p_{11_{exp}}$ to generate an error value. The average error is then determined by summing over the entire error distribution and dividing by the total number of data points. Figures 13 and 14 show a comparison of the error merit function (inverse mean squared error) for the p_{11} phase function compared with those computed for the p_{12}, p_{33} and p_{34} phase functions. There is close agreement between the p_{11} and p_{12} phase functions in predicting the most likely particle size; this is especially true for the 1 micron diameter particles. In that case, the p_{33} and p_{34} phase functions coincide but appear to show an overestimate of the particle size by about 1%. [5] showed that while the p_{22} phase function is sensitive to concentration (due to multiple scattering), single scattering theory shows it is independent of size and index of refraction, and thus we will not use it in our error analysis.

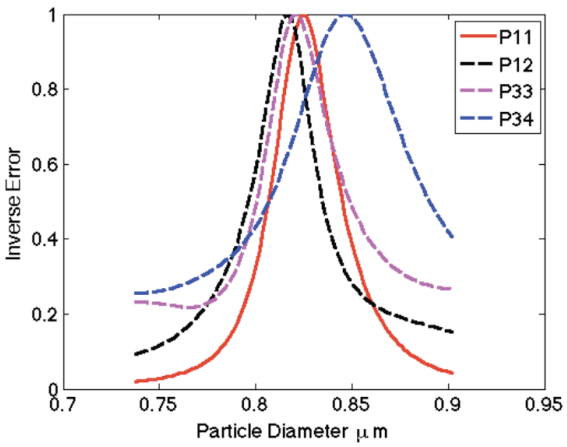

Figure 13. Comparison of error merit functions (inverse error) for particle sizing for the nonzero valued phase functions for ensemble of 820 nm polystyrene latex spheres.

Our minimum error is found at a particle diameter of 825 nm, which is well within the 3% size distribution. The same error analysis performed on the dataset for 1 μm diameter particles is shown in Figure 14.

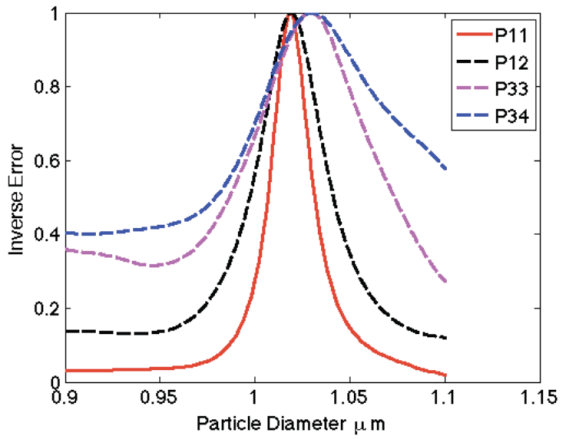

Figure 14. Comparison of error merit functions (inverse error) for particle sizing for the nonzero valued phase functions for ensemble of 1 μm polystyrene latex spheres.

For the particle ensembles of 820 nm and 1 μm, we record peaks in our merit function at particle diameters of 825 nm and 1.01 μm, respectively, both well within the 3% size distribution reported by Duke Scientific.

If one wants to characterize other physical independent parameters of an ensemble (e.g., index), we can expand the merit function by either adding the index of refraction as a second independent variable with the same phase function, or by adding additional phase functions. In either case one would then perform the error analysis in multiple dimensions.

8 Conclusion

We have introduced a One Dimensional Poincare Beam for use in remote sensing technologies. Furthermore, we have derived consistent and accurate phase matrix retrieval techniques and have validated the results with Mie theory. Using this, we have demonstrated that it is possible to determine the diameter of the particles within 1%. However, there is a depolarization contribution to the experiment, which cannot be directly quantified by simply using a linear analyzer at the output. Better polarimetry at the detector plane would allow us to discern whether the depolarization contribution is due to multiple scattering or a stray unpolarized signal within the scattering cell. While diluting the sample can mitigate multiple scattering, we have found it difficult experimentally to achieve the single scattering limit. The current technique is also limited by the accuracy of the analyzer before the detector. Since the uncertainty in the analyzer position (about 1 degree) makes it difficult to have absolute accuracy in the analyzer position. In other papers, we explore a new method of polarimetry, which is better equipped to correct some of these errors and account for light that has been multiply scattered.

References

[1] C.F. Bohren and D.R. Huffman, *Absorption and Scattering by Small Particles*, Wiley Interscience, New York, NY, 1983.

[2] M. Kerker and M.I. Hampton, "The use of unfiltered light in determining particle radius by the polarization ration of the scattered light," *Journal of the Optical Society of America*, Vol. 43, No. 5, 1953.

[3] M. Kerker and V.K. Lamer, "Aerosol studies by light scattering. I. Particle size distribution by polarization ratio method," *Am. Chem. Soc.*, Vol. 72, 3516 1950.

[4] H.C. Van de Hulst, *Light scattering by small particles*, Leiden Observatory (Dover Publications, Inc.), NY, 1957.

[5] J. Hansen and D. Travis, "Light scattering in planetary atmospheres," *Space Science Reviews*, Vol. 15, pp. 527-610, 1974.

[6] A.J. Hunt, D.R. Huffman, and R. Donald, "A new polarization-modulated light scattering instrument," *American Institute of Physics*, Vol. 44, No. 12, 1973.

[7] J.S. Tyo, "Review of passive imaging polarimetry for remote sensing applications," *Applied Optics*, Vol. 44, No. 22, 2010.

[8] J.V. Martins, "Airborne open polar/imaging nephelometer for ice particles in cirrus clouds and aerosols," A Research Proposal to the Department of Energy, 2010.

[9] J.V. Martins et al, "The next generation of UV/VNIR/SWIR wide FOV hyperangular imaging polarimeter for aircraft and space applications," Am. Geophys. Union, Fall Meeting, Abstract A21J-08, San Francisco, CA, 2010.

[10] O. Dubovnik et al, "Variability of absorption and optical properties of key aerosol types observed in worldwide locations," *J. Atmospheric Sciences*, Vol. 59, 590, 2001.

[11] G. Miecznik et al. "Sensitivity metric approach for retrieval of aerosol properties from multiangular and multispectral polarized radiances," *Applied Optics*, Vol. 44, 4196, 2005.

[12] M.I. Mishchenko et al, "Monitoring of aerosol forcing of climate from space: Analysis of measurement requirements," *J. Spectr. Rad. Trans.* Vol. 88, 149, 2004.

[13] M.S. Quinby-Hunt, "Polarized light scattering by aerosols in the marine atmospheric boundary layer," *Applied Optics*, Vol. 36, No. 21, 1997.

[14] T.G. Brown, "Unconventional polarization states: Beam propagation, focusing, and imaging," *Progress in Optics*, Vol. 2, 2011.